



Deformation mechanism of various Sn-xBi alloys under tensile tests

Shanshan Cai¹ · Xiaobin Luo¹ · Jubo Peng¹ · Zhiqi Yu² · Huiling Zhou² · Ning Liu² · Xiaojing Wang²

Received: 11 February 2021 / Revised: 22 February 2021 / Accepted: 23 February 2021 / Published online: 11 March 2021
© The Author(s), under exclusive licence to Springer Nature Switzerland AG 2021

Abstract

In this study, the thermal properties, mechanical properties, and microstructure evolution of Sn-xBi ($x=0, 10, 17, 20, 30, 40, 50,$ and 58 wt.%, respectively) alloys were investigated via differential scanning calorimetry, scanning electron microscope during and after tensile test. The results reveal that the shapes of precipitated Bi particles relate to the cooling rate, that is, sphere in water cooling condition and short rod like cooled in air. Beta tin phase strengthened by Bi particle precipitation offers superior performance than Sn-Bi eutectic structure. The result also clearly demonstrates the deformation and fracture modes of Sn-Bi alloys with different microstructure through in situ observations during tensile loading. The deformation of Sn-17Bi alloy deforms based on the grain boundary diffusion. For Sn-58Bi alloy, the deformation is mainly resulted by grain boundary sliding during even deformation stage and the phase sliding between Bi-rich and Sn-rich phase boundary after necking. And the latter accounts for the majority. Sn-50Bi alloy deforms through grain boundary sliding of eutectic phase and phase boundary sliding between beta tin phase strengthen by precipitated Bi and eutectic phase. Moreover, Sn-rich phase works as floating grains, does not participate in the deformation, but provides sliding interface with the eutectic part, which promotes the continuous plastic deformation.

Keywords Sn-Bi alloy · Beta tin · Mechanical properties · Tensile deformation

1 Introduction

Since the replacement of lead-free solder in electronic industry, Sn-Ag-Cu (SAC) alloy became the mainstream alloy of electronic manufacturing for surface mount technology procedure. However, the heat input of SAC solder fabrication has been a concern always due to the high reflowing temperature (not lower than 260 °C) [1]. This makes thin and large chips prone to warping [2, 3]. Sn-Bi alloy with lower melting point, which was shelved in the early period of lead-free solder research, has come back to attention [4–6]. For the lower reflowing temperature enables the usage of cheaper substrates, which may significantly reduce the materials, energy, and fabrication costs. This makes the low soldering

solution based on Sn-Bi solder a very competitive proposal. Based on the roadmap of iNEMI (International Electronics Manufacturing Initiative) 2015, a lower-temperature micro-soldering solution (1–20% lower than the melting point of Sn-3.0Ag-0.5Cu alloy) has been expected to fulfill within the following 10 years. Sn-Bi alloy is the first choice because of its low cost compared with Sn-In (another low temperature solder for lower temperature, regardless of cost).

According to the content of bismuth in alloy, the studies of Sn-Bi alloy involve two categories. One is the property adjustment based on Sn-Bi eutectic alloy or near eutectic alloy [7]. It includes the micro alloying process and the nano-particle addition [8]. For example, the micro alloying elements of Ag [7], Cu [7, 9, 10], Ni [11], Cr [12] etc. are mainly as a compound formation element added to strengthen the solder by dispersion strengthening; elements Sb [13, 14], Zn [15–17], and In [18–21] additions may either solute in beta tin or form the IMC particles with Bi and vice versa.

The other is that bismuth is added into tin-based alloy as strengthening element to form tin bismuth alloy. Actually, Bi has been added to Sn-Ag, Sn-Cu, Sn-Zn, and Sn-Ag-Cu solders to improve the wetting behavior, strengthening, and melting properties. It is found that Bi addition to SAC solder

✉ Jubo Peng
1367558560@qq.com

✉ Xiaojing Wang
wxj@just.edu.cn

¹ Yunnan Tin Group (Holding) Co. Ltd, Kunming 650000, China

² Jiangsu University of Science and Technology, Zhenjiang 212003, China

could improve the mechanical properties [22] including the creep and fatigue resistances [23–25]. And 1 or 4 wt.% Bi doped into Sn-Zn alloy could also enhance the mechanical properties of Sn-Zn solder [24]. Based on the previous researches, Bi addition may improve the thermal, mechanical, and deformation behavior of Sn-based alloys. Therefore, when bismuth is added to pure tin to form Sn-Bi non-eutectic alloy, what is the appropriate bismuth content? Recent results and our previous work confirm that the mechanical properties of eutectic composition are lower than that of beta-Sn-based Sn-Bi alloy [9, 26, 27]. This explains that the content, morphology, and size of Bi element play an important role on the solder performance [28, 29]. Actually, during the low-temperature fabrication procedure for temperature sensitive components or LED connections, decreasing Bi content from the eutectic content, 58 wt.% to 40, 35, 30 wt.% and even 17 wt.%, with minor Cu or Ag doped has been confirmed to be useful to meet the step soldering procedure and relieve the Bi phase segregation along the solder/substrate interface [29–32]. And, taking Bi as a source for precipitating hardening for beta tin phase may provide an efficient result for Sn-Bi solders. But the basic reasons for this hardening of beta tin and the deformation behavior of hypoeutectic Sn-Bi alloys desperately need further investigations to provide a better understanding for Sn-Bi solder solution optimization.

2 Experimental procedure

Sn-*x*Bi alloys were prepared by putting Sn (99.99%) and Bi (99.99%) metals in a quartz tube for 15 mm in diameter, melting at 600 °C for 60 min. During melting, the melts were stirred at least 3 times before cooling the quarter tube

in water. The sample alloy fabrication process is shown in Fig. 1. The samples for microstructure and phase identification were prepared near the ingots bottom surfaces. Then, the scanning electron microscopy equipped with energy dispersive X-ray spectrometry was used for the microstructure observation and phase identification, respectively.

The thermal behavior of the alloys was investigated by using differential scanning calorimetry (DSC) measurement at heating and cooling rate of 2 °C/min under Ar gas atmosphere.

The tensile tests for evaluation of the mechanical properties were performed in a universal testing machine at a speed rate of 6 mm/min. All the alloys were machined into specimens with 2 mm² cross section area and 10 mm gauge length, as shown in Fig. 2. Stress-strain/tensile-displacement curves for at least three specimens for each alloy were conducted at room temperature. The ultimate tensile strength (UTS) and elongation (EL) were also reported in scatter curves for better understanding the results. The deformation and fracture surfaces of the selected Sn-10Bi, Sn-17Bi, Sn-40Bi, and Sn-58Bi specimens were observed in details through scanning electron microscopy during and after tensile test. During the test, displacement loading was carried out in several steps followed by SEM surface observation subsequently. So, the surface observations were implemented after 1 mm, 2 mm, and 3 mm (2.5 mm for Sn58Bi alloy) displacement loading, respectively, accompanied by a fracture surface observation after fracture. Samples were marked before deformation observation for tracking the same observation position during tensile test. The displacement load curves in “Deformation during tensile test” were selected from the normal tensile test (results from Fig. 9) of the same alloy for a clear demonstration of deformation behavior.

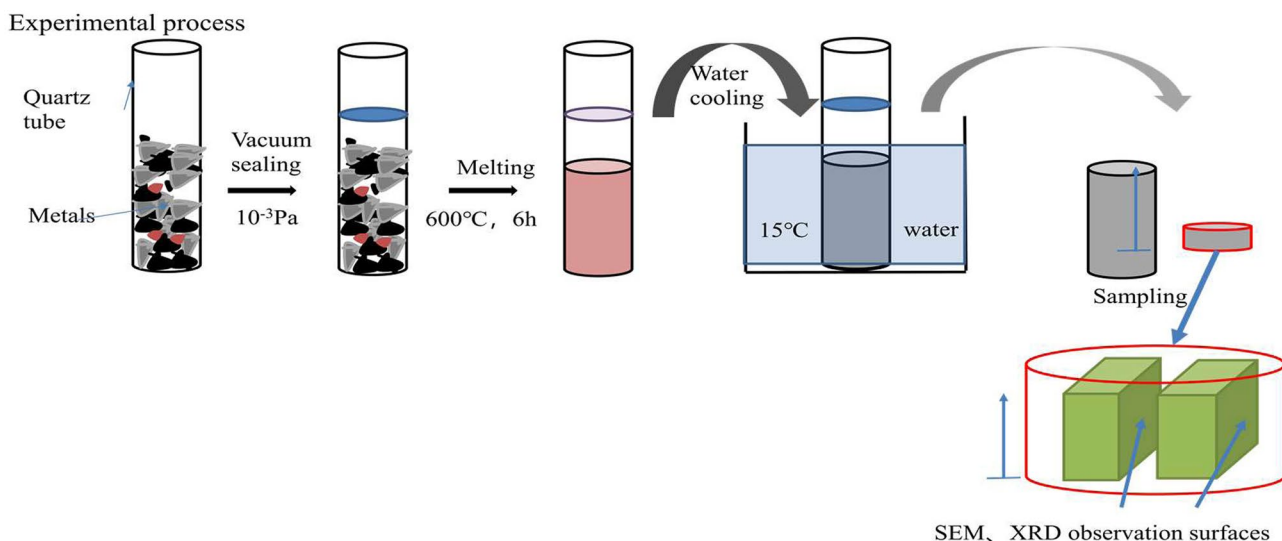
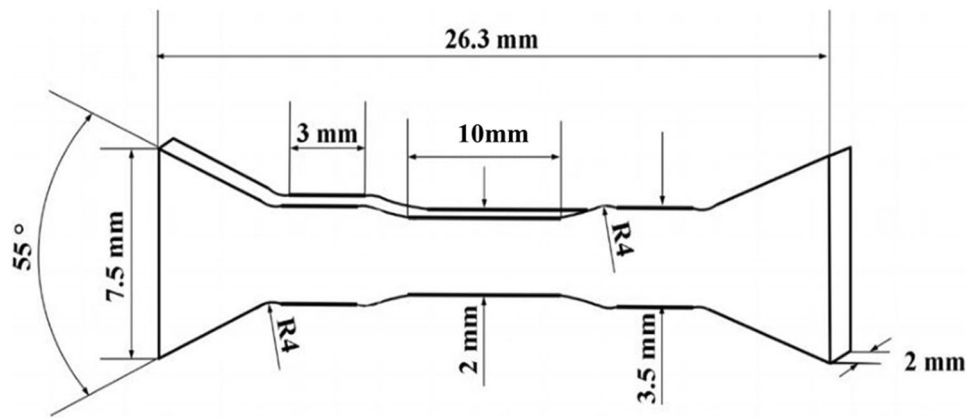


Fig. 1 The fabrication procedure of Sn-*x*Bi alloys (sketch not in scale)

Fig. 2 The schematic illustration of the tensile sample



3 Results and discussion

3.1 Thermal behavior

Figure 3 displays the DSC curves of Sn-xBi alloys during heating and cooling processes at a scanning rate of 2 °C/

min. There are two peaks shown in both heating and cooling curves except for Sn-58Bi eutectic alloy. According to the Sn-Bi phase diagram, the peak of Sn-58Bi represents the eutectic transformation at 138 °C (136.25 °C in this study) under equilibrium phase transformation: L → eutectic (Bi-rich + Sn-rich) phase. The undercooling is about 7.05 °C

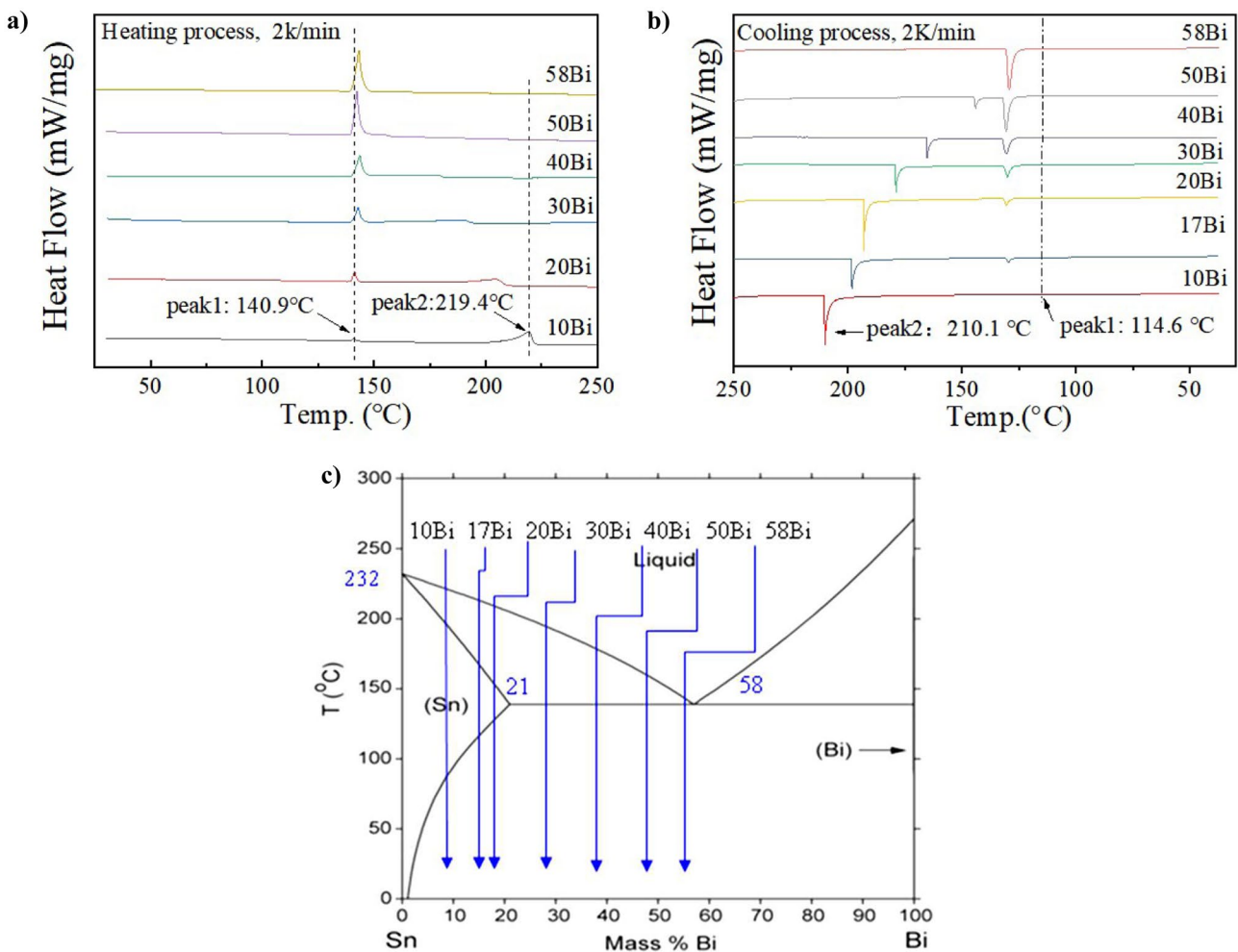


Fig. 3 DSC curves and phase diagram

calculated from the peak temperature during heating minus the peak temperature cooling down divided by 2.

The thermal properties of other Sn-*x*Bi alloys are quite different from those of Sn-58Bi alloy. For Sn-10Bi alloy, there are two exothermic peaks on the DSC cooling curve. The higher temperature peak (numbered peak 2) represents primary beta tin phase precipitation with minor Bi dissolved in. And with the precipitation of primary beta phase during cooling down, the concentration of bismuth in the remnant liquid increases continuously. Finally, when temperature reaches peak 1 as shown in Fig. 3, the liquid phase with more bismuth finally transforms into beta tin phase. The solid solubility of bismuth in tin decreases with further decrease of temperature, and bismuth particles precipitate from the primary beta phase gradually. Thus, the peak 1 of Sn-10Bi should represent the reaction: Beta-Sn (high temperature) → Beta-Sn (low temperature) + Bi. Which occurs about 114.6 °C according to the cooling dsc curves. That is, the liquid to solid phase transition process can be described as follows: $L_1 \rightarrow L_2 + (\text{primary Sn-rich}) \rightarrow \text{Sn} \rightarrow \text{Sn} + \text{Bi}$ precipitates.

According to Sn-Bi phase diagram, the maximum solubility of Bi in solid beta Sn is 21 wt.%. Thus, Sn-20Bi should share the similar phase transformation sequence with Sn-10Bi (see Fig. 3c). Actually, from the DSC curves of Sn-*x*Bi alloys, the peak characteristics of Sn-20Bi alloy are more similar to those of Sn-30Bi, Sn-40Bi, and Sn-50Bi alloys. They all have an exothermic peak close to eutectic temperature 136.25 °C in this study and usually 138 °C. This is because the Sn-*x*Bi alloys in this study are prepared via water cooled solidification process, which makes the undercooling about 5 °C. So, the phase precipitation controlled by diffusion is inhibited, and the eutectic transformation of Sn-Bi occurs.

Thus, the two peaks of DSC curves for Sn-20Bi, Sn-30Bi, Sn-40Bi, and Sn-50Bi alloys, peak 2 represents the precipitation of Sn phase from liquid metal, while peak 1 displays eutectic transformation. The sequence of phase transition could be described as follows: $L_1 \rightarrow L_2 + (\text{primary Sn-rich phase}) \rightarrow \text{eutectic structure (Bi-rich phase} + \text{Sn-rich phase)} + (\text{primary Sn-rich phase} + \text{Bi precipitates})$. And the under cooling is in the range of 5.7~13.15 °C, as shown in Table 1.

Table 1 Thermal properties of Sn-*x*Bi alloys

Alloys	Thermal properties(°C)						
	Heating			Cooling		Under cooling	Under cooling
	Peak1	Peak2	Melting range	Peak1	Peak2	Peak1	Peak2
Sn-10Bi	140.9	219.4	78.5	114.6	210.1	13.15	4.65
Sn-17Bi	141.4	204.9	63.5	130.5	192.9	5.7	6
Sn-30Bi	143	191.1	48.1	130.0	178.9	6.5	6.1
Sn-40Bi	143.7	177.1	33.4	130.5	165.2	6.6	5.95
Sn-50Bi	142.5	153.4	10.9	130.5	144.0	5.95	4.7
Sn-58Bi	143.3			129.2		7.05	136.25

Table 2 Solidification properties of Sn-*x*Bi alloys

	C_s^* (the start point for solidification)	Eutectic fraction (f_s when $C_L^* = 0.58$)
Sn-10Bi	3.6%	6.2%
Sn-17Bi	6.2%	12.6%
Sn-20Bi	7.2%	18.5%
Sn-30Bi	10.8%	35.2%
Sn-40Bi	14.4%	57%
Sn-50Bi	18%	79%

3.2 Microstructure

As shown in Sn-Bi binary phase diagram in Fig. 3c, six hypoeutectic alloys of Sn-10Bi, Sn-17Bi, Sn-20Bi, Sn-30Bi, Sn-40Bi, and Sn-50Bi are indicated, respectively. These alloys are discussed in detail to understand the solidification behavior. The Sn-Bi eutectic content calculated based on Scheil's model for Sn-*x*Bi alloys is shown in Table 2. And the Scheil Gulliver equation is related to the redistribution of solute elements in the solidification process of alloy, also known as the lever law of non-equilibrium crystallization, see Eq. 1. It describes the redistribution law of solute under the condition of non-diffusion of solid phase and uniform mixing of liquid phase in a wide range of experimental conditions.

$$C_s^* = k_0 C_0 (1 - f_s)^{(k_0 - 1)} \quad (1)$$

At a certain moment during solidification, the components at the interface of solid-liquid phase are C_s^* and C_L^* , and the corresponding mass fractions are f_s and f_L . The original composition of the alloy is C_0 . For Sn-Bi hypoeutectic alloys, the calculations were conducted by considering the eutectic temperature of 138 °C, where $k_0 = C_s/C_L = 21/58 = 0.36$, the constant equilibrium partition coefficient. And C_s is the solid composition (limit of solid solubility) and C_L is the liquid compositions (limit of eutectic compositions), respectively. When $f_s = 0, C_s^* = k_0 C_0$, so for Sn-40Bi alloy, $k_0 = 0.36, C_0 = 0.4$, then $C_s^* = 0.36 \times 0.4 = 14.4\%$. Similarly, for Sn-10Bi (Sn-17Bi, Sn-20Bi, Sn-30Bi, Sn-40Bi, and Sn-50Bi)

alloy, the $C_s^* = \left(\frac{21}{58}\right) \times 0.1(0.17, 0.2, 0.3, 0.4, 0.5, 0.56) = 0.036$ (0.062, 0.072, 0.108, 0.144, 0.18). For the Bi content, liquid phase can be expressed by the following equation,

$$C_L^* = C_0 f_L^{(k_0-1)} \quad (2)$$

From Eq. (2), it is easy to find if the concentration of bismuth reaches 58 wt.% in liquid phase (the eutectic content of Sn-Bi alloy), $C_L^* = 0.58$, the Bi content in the residue liquid during solidification is about 6.4%. That is, the residue of the liquid fraction will experience the eutectic phase transformation which will not occur in equilibrium condition. Thus, the eutectic phase in Sn- x Bi alloys can be listed in Table 2. This could explain why the eutectic microstructure and the unusual DSC peak have been shown in the previous results about Sn-20Bi alloy.

As shown in Fig. 4, the solidified microstructures of the hypoeutectic Sn- x Bi alloys observed consist of eutectic mixture and Sn-rich dendrites decorated by Bi precipitates in their own core, generally. These two phases have different

lattice structures, the Bi-rich phase is rhombohedral and the Sn-rich phase is body centered tetragonal. During cooling, the solid solubility of bismuth in beta tin decreasing explains the Bi particle precipitation within the beta Sn-rich regions. It can be seen from the previous analysis that eutectic phase exists in all alloys during non-equilibrium solidification. For Sn-10, 17Bi, 20Bi alloys (Fig. 4a–c), the microstructure can be seen as the beta tin base with precipitated Bi particles decorated on. For Sn-30Bi, the eutectic phase is about 35.2%, which has not connected to form net structure like Sn-40Bi (Fig. 4d). Thus, the microstructure of Sn-40Bi and Sn-50Bi alloys mainly contains Sn-Bi eutectic phase and beta tin with Bi particles precipitated during cooling, as seen in Fig. 4e.

Figures 4f and 5 show that the microstructure of Sn-58Bi contains three eutectic characteristic structures: finer (in dashed black lines), coarser eutectic zones, and fish bone structure, indexed by black arrow. Sn- x Bi alloys, as aforementioned, are characterized by quite complex eutectic structures. The structure variation from lamellar

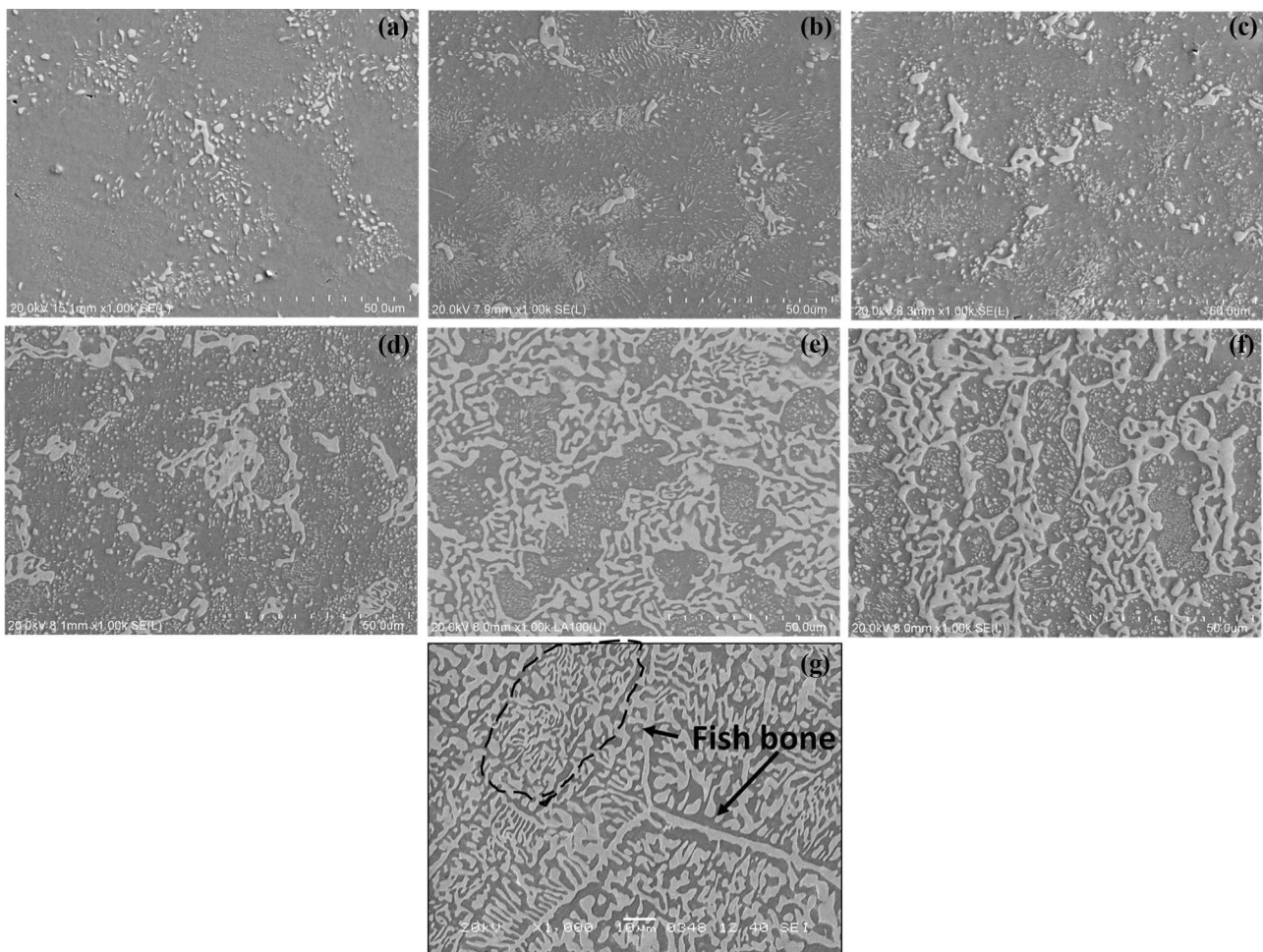


Fig. 4 Microstructures of **a** Sn-10Bi, **b** Sn-17Bi, **c** Sn-20Bi, **d** Sn-30Bi, **e** Sn-40Bi, **f** Sn-50Bi, and **g** Sn-58Bi

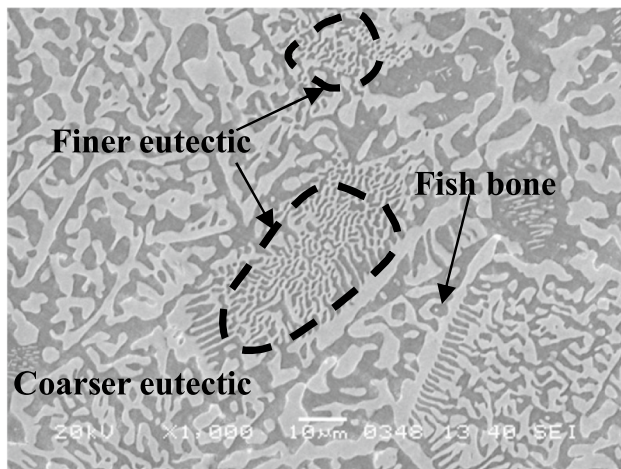


Fig. 5 Microstructure of Sn-58Bi alloy

morphology (quasi-regular) to a more complex-regular structure strongly depends on the thermal parameters under solidification process [9, 33]. For example, a much higher cooling rate is conducive to a more complex microstructure. The coarser and finer microstructure regions shown in the present results could be ascribed to thermal instabilities which is associated with the local heat flow during cooling down. That is a typical non-steady state cooling condition. That is, the finer eutectic features could be formed in some certain sites, surrounded by much coarser structures, driven by the thermal instabilities with quicker cooling rates. In Fig. 4, both finer and coarser eutectic regions are highlighted in SEM images, displaying both Sn-rich and Bi-rich phases. Generally, the finer eutectic emerges like isolated “islands” among the eutectic mixtures and beta-tin rich dendrites [28]. And a typical “fishbone” eutectic structure is also observed in Fig. 4. This structure usually preferred to appear adjacent to the lamellar structure of Bi-rich phase, as seen in Figs. 4 and 5 indicated by black arrows. The fishbone-like structure in Sn-58Bi specimens appears as an isolated area from the two different scales of lamellar eutectic phases. Thus, the microstructures, the second or third phases in size of Sn-*x*Bi alloys, are summarized in Table 3.

Additionally, the distribution and fraction of Bi precipitates within the dendritic Sn regions are found uneven. Those Bi particles display both spherical and rod-like (ellipsoidal in Ref. [9, 28]) morphologies as shown in Fig. 6.

This phenomenon should be related to the temperature field during solidification. When the temperature is steady during cooling down and long enough for the Bi Particle to grow driven by the temperature difference, the Bi particle could be rod like which means the Bi phase were growing along the same direction[34]. When changing the cooling rate from water cooled to air cooled solidification conditions, the cooling rate and temperature gradient decrease, while the concentration gradient increases by at least an order of magnitude, which assures the material transport distance increases. This makes the precipitation of bismuth particles form in a shape of elliptical or short rod geometry, as shown in Fig. 7.

3.3 Mechanical properties

3.3.1 UTS and elongation

Figure 8 shows ultimate tensile strength (UTS) and elongation values of Sn-*x*Bi alloys. It is found that UTS of the alloy increases with Bi content firstly, reaching the maximum value of about 81 MPa when Bi content is 17 wt.%; with Bi content further increasing from 17 to 58 wt.% of eutectic composition, UTS shows a downward trend, from 81 to 60 MPa. Correspondingly, the elongation decreases with Bi content increasing, from 61% of pure tin to about 21% of eutectic alloy. This is consistent with the UTS curves changing with Bi content from Rachal et al. [29], showing that Sn-Bi alloy with 40 wt.% Bi content could be a better base alloy to adjust the mechanical properties of Sn-Bi alloy.

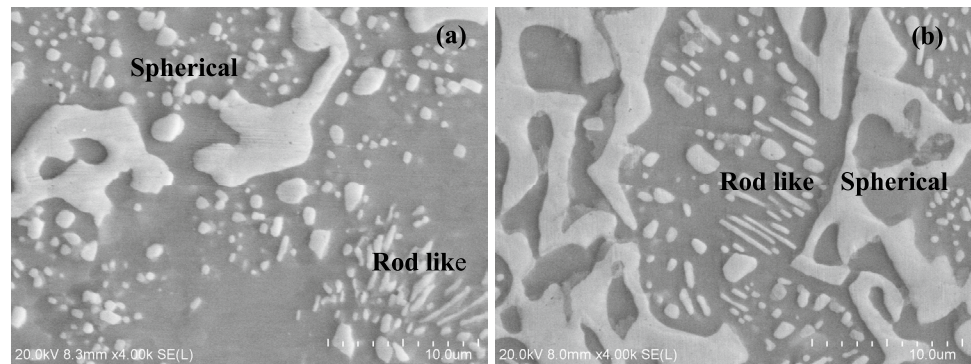
3.3.2 Deformation during tensile test

For better understanding the deformation behavior of Sn-*x*Bi alloys. Sn, Sn-17Bi, 50Bi, and 58Bi alloys were selected for further deformation observation. As shown in Figs. 9, 10, 11, and 12, all the tensile curves contain a linear elastic

Table 3 Microstructure properties of Sn-*x*Bi alloys

Alloys	Base	The second or third phases
Sn	Beta tin grain 46 µm	
Sn-10Bi	Beta tin (43.4 µm)	Bi particles under 1 µm + (eutectics)
Sn-17Bi	Beta tin (40.1 µm)	Bi particles (about 1 µm) + (eutectics)
Sn-20Bi	Beta tin (32.1 µm)	Bi particles (1 µm) + eutectics
Sn-30Bi	Beta tin (20.3 µm)	Bi particles (2 µm) + eutectics
Sn-40Bi	Sn-Bi eutectic	Beta tin (11.2 µm) with 2 µm Bi + eutectics
Sn-50Bi	Sn-Bi eutectic	Beta tin (8.1 µm) with dot or short rod Bi + eutectics
Sn-58Bi	Sn-Bi eutectic	Finer + coarser structure + fish bone

Fig. 6 Spherical and ellipsoidal morphologies of Bi particles in **a** Sn-20Bi and **b** Sn-50Bi alloys



stage, plastic rising, and a load resistance decay stage after necking. When the tensile displacement is 1 mm, the tensile sample for pure tin already entered the stage of uniform plastic deformation. The grain morphology of the sample surface is clearly visible. This is due to the local cracks caused by the uneven deformation of grains with different orientations at the grain boundary [29][35][36][37]. At this time, the grains keep equiaxed shape. When the displacement is further increased to 2 mm, it is found that the grains extend into a strip shape along the loading direction. For example, the grain boundaries of A, B, and C are flattened in Fig. 9. For this kind of banded morphology, it might be resulted by the deformation at the grain boundary is faster than that inside the grain. According to the tensile results dependent on strain rate and temperature, the activation energy for pure tin at room temperature, lower strain rate, is about 37 kJ/mol. And the activation energy of bulk diffusion of Sn is about 100–130 kJ/mol [37] [38], that of grain boundary diffusion of pure Sn is about 30–40 kJ/mol [39]. Thus, it should be the grain boundary diffusion-guided deformation for pure tin based on the data and the deformation observation. This also was confirmed by the TEM observation during tensile fracture in pure tin [40]. The vacancy diffusion driven the micro-voids nucleated, finally linked up to form the cracks propagation [40, 41].

We further find that a small grain appears between the three grains A, B, and C, see Fig. 9a–c. This phenomenon may be due to the grain boundary sliding which leads to

the appearance of the grain behind, or the recrystallization which resulted by the appearance of a new grain at the trigeminal grain boundary [42]. Combined with the tensile curve in Fig. 9d, it can be seen that the plastic deformation of pure tin mainly comes from the uniform deformation before necking. The ability of diffusion and transfer of deformation in the alloy is better. Once necked, the crack propagates rapidly and the material breaks subsequently as shown in Fig. 9e. The fracture surface presents a fracture line showing a strong plastic fracture.

In addition, the area of the shadow part under the force-displacement curve is obtained by integrating the force with the displacement, that is, the energy required in the stretching process is 559.51 mJ.

For Sn-17Bi solder, when the tensile sample enters plastic deformation stage after 1-mm displacement along tensile direction, some grain boundaries become visible, see Fig. 10a. When the displacement is further increased to 2 mm, the grain boundary becomes clearer, and the deformation of the alloy is coordinated between grains. The bismuth phase distributed on beta Sn base no matter the eutectic fraction or precipitated particles deforms within beta tin. The grain deformations with different orientations become uneven. Additionally, voids can be seen at the grain boundaries in Fig. 10 a–c and f, g, which further validates the atom diffusion at the grain boundaries in fracture process. Comparing with Fig. 10 e and f, it can be seen that some grains appear at the grain boundaries shown by black arrows, which

Fig. 7 Microstructure of Sn-40Bi alloy under **a** air-cooled condition and **b** cooled in water

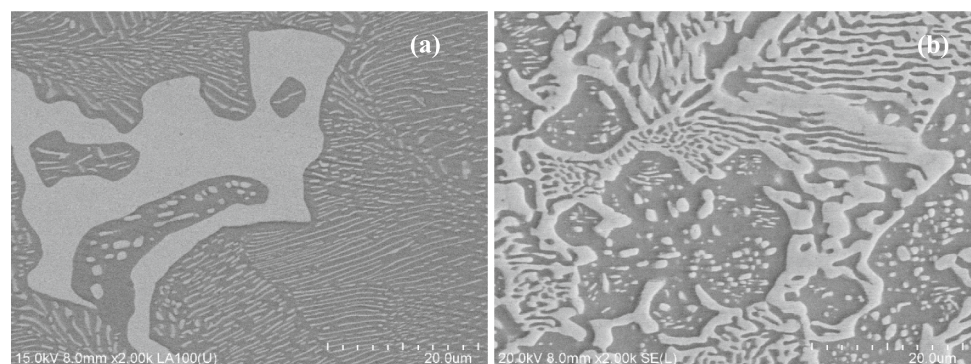
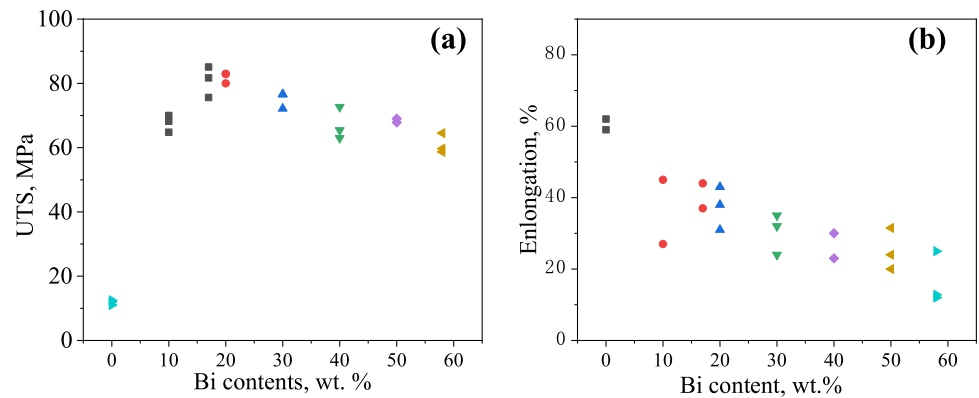


Fig. 8 Tensile properties of Sn-xBi alloy: **a** UTS and **b** elongation



may be due to recrystallization. With the fracture continuing, by 3 mm in tensile direction, micro-cracks nucleated at the voids, which finally connected to drive the crack propagation furthering the tensile fracture. The fracture surface observation in Fig. 10e displays a plastic characteristic of dimples generally. Therefore, the grain boundary should be

the location of crack initiation [40]. And this crack finally connected within beta tin phase forming the dimple ridge, showing a fracture surface in Fig. 10e. The dimple size and grain size should be comparable, 46 μm or so.

Figure 11 shows the force-displacement curve, morphologies during and after tensile deformation of Sn-50Bi

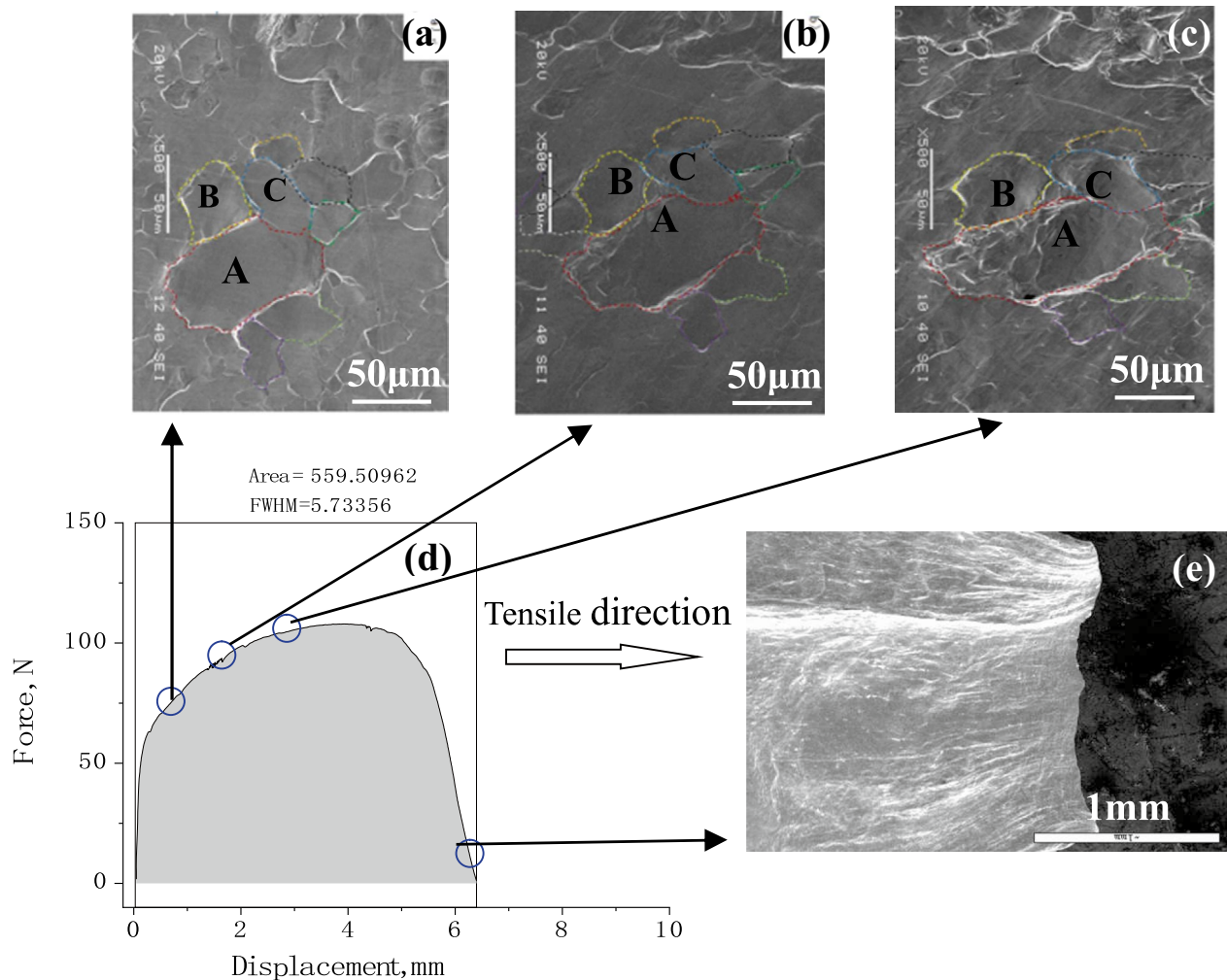


Fig. 9 Beta tin deformation during tensile test after **a** 1 mm, **b** 2 mm, and **c** 3 mm displacements, **d** force-displacement curve, and **e** fracture surface (side)

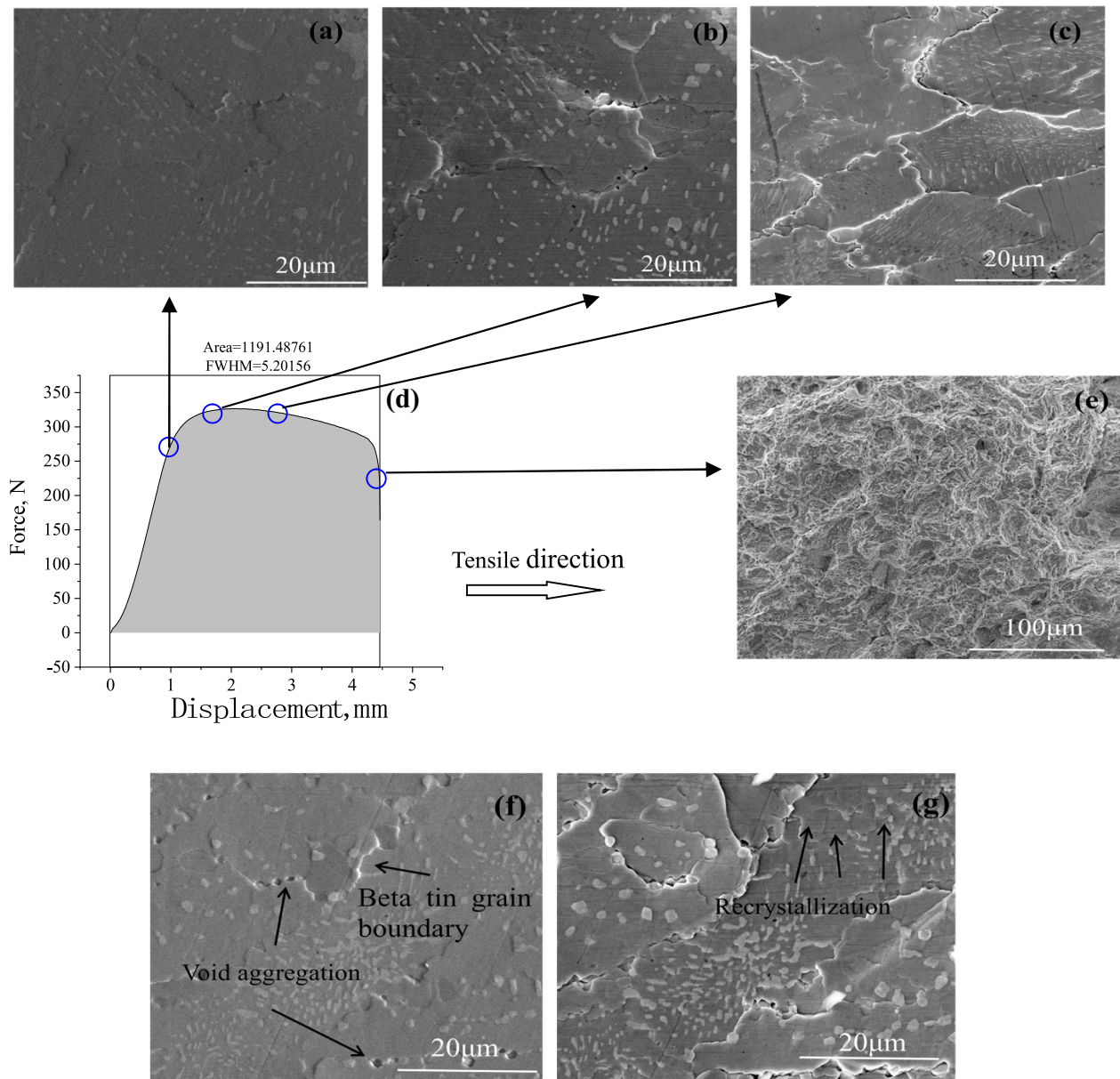


Fig. 10 Sn-17Bi alloy during tensile test after **a** 1 mm, **b** 2 mm, and **c** 3 mm displacements; **d** force-displacement curve, **e** fracture surface, **f** 1 mm, and **g** 2 mm displacements under higher magnification images

alloy. During the tensile process, when the displacement reaches 1 mm, the uneven deformation appears on the alloy surface, as shown in Fig. 11a. The deformation in Sn region and eutectic region with different orientations shows great difference. Phase boundary slip occurs between the phase interfaces of beta tin and eutectic regions (see Fig. 11a2). And there are steps shown between eutectic phases with different orientations (called grain usually), indicating the inconsistent deformation between them. Further deformation strengthens this feature, as shown in Fig. 11b, c.

Additionally, it is noted that the shape of beta tin phase remains unchanged during the displacement that varies from 1 mm, 2 mm, and 2.5 mm. This zone works as a kind of floating grains during the tensile deformation until the end of deformation. Within eutectic regions, the uneven deformation results in the concave convex between the Sn-rich and Bi-rich lamellar phases. The tin rich phase has protruded on surface and bears the main part of the deformation, shown in higher magnification images (Fig. 11a2~c2). At the displacement of 2.7 mm, the sample fractured with the total energy of 576.83 mJ.

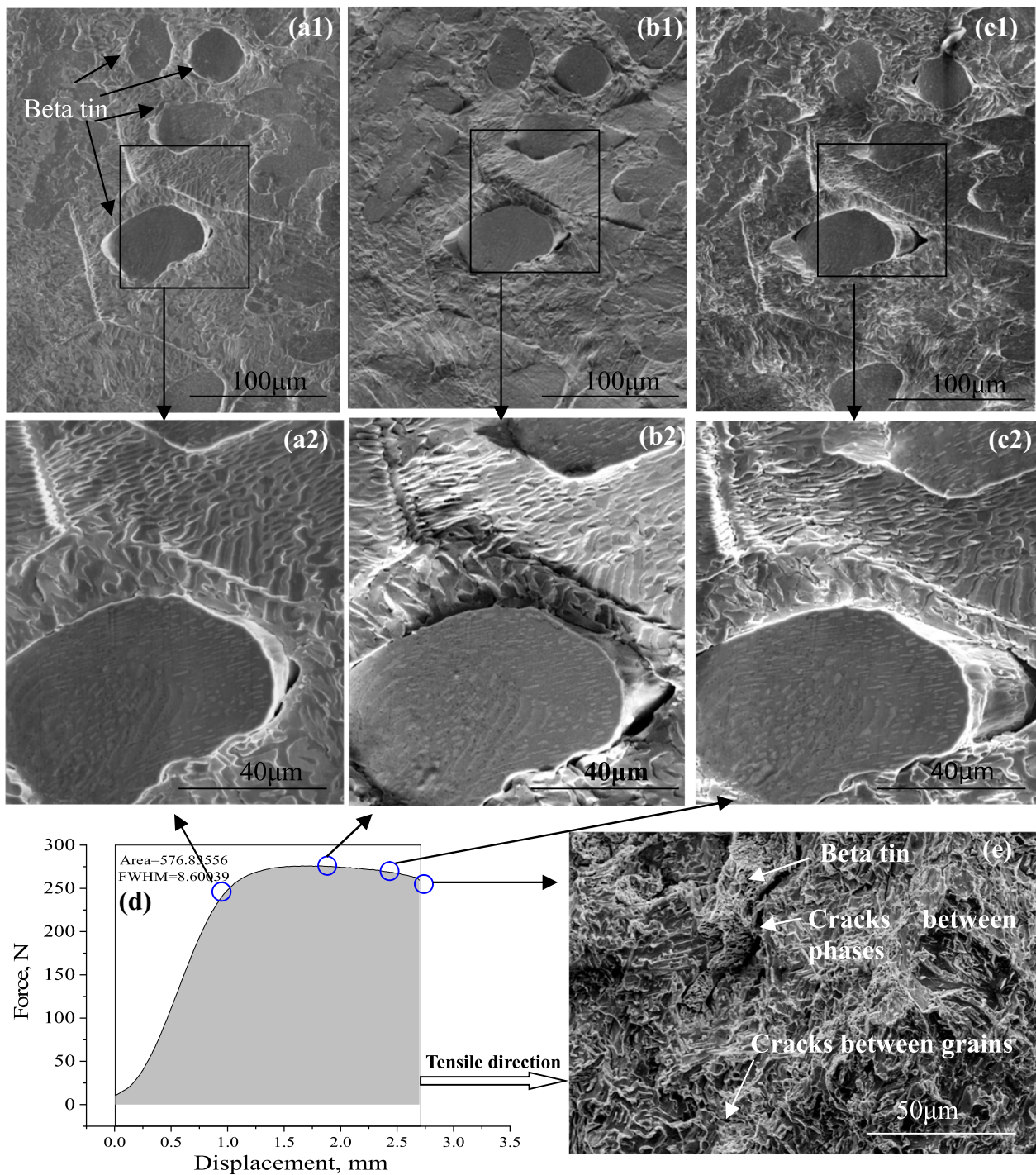


Fig. 11 Sn-50Bi deformation during tensile test after **a1, a2** 1 mm, **b1, b2** 2 mm, **c1, c2** 2.5 mm displacements, **d** tensile curve, and **e** fracture surface after tensile test

The fracture surface shows beta tin-based regions with very fine dimples and the eutectic fracture regions, quite flat in general. From the microscopic point of view, the eutectic fracture zone is composed of Bi-rich region with cleavage smooth facet morphology and Sn-rich region bearing deformation (Fig. 11e).

In addition, two kinds of cracks can be seen on the fracture surface, one is the large cracks between phases; the other is the micro cracks between eutectic grains.

For Sn-58Bi alloy, the grains with preferred orientation deform first, along with the sliding of phase boundary in the grains, which further promotes the deformation of slip

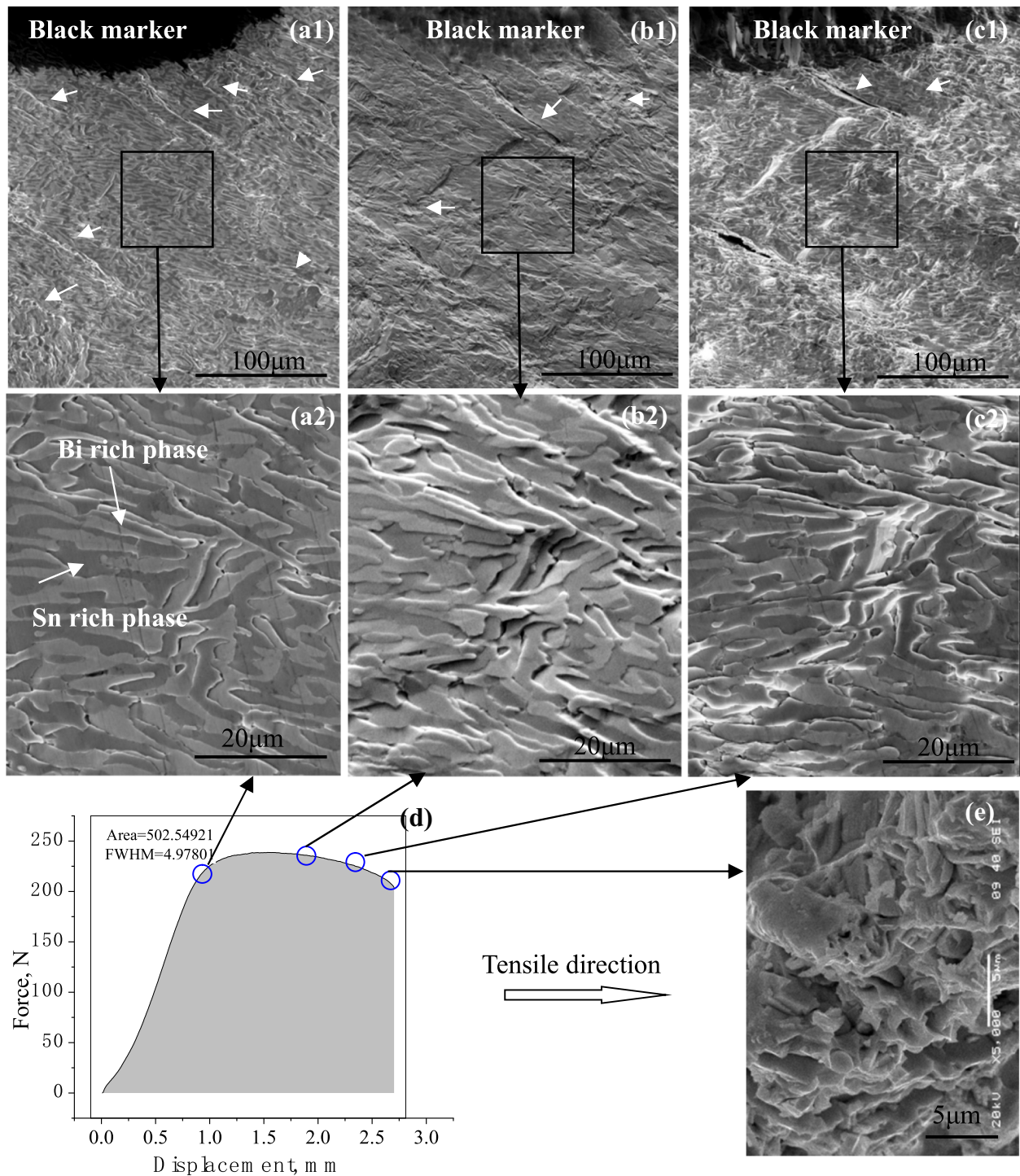


Fig. 12 Sn-58Bi deformation during tensile test: **a1, a2** 1 mm, **b1, b2** 2 mm, and **c1, c2** about 2.5 mm displacements, **d** tensile curve, **e** fracture surface after tensile test

band along the tensile direction, as the white arrow shown in Fig. 12a–c. At the initial of tensile test, the grain boundary first slides where most of the phase boundary does not change at all. With the displacement reaching 1 mm, the phase boundary slides directly accompanied by the deformation of

Sn-rich phase, see Fig. 12b. There are obvious sliding steps at the interface of Sn-rich and Bi-rich phases showing up. With tensile displacement furthering, the deformation of Sn-rich phase intensifies, while the fracture of Bi-rich phase occurs, and the whole alloy appears to collapse. The broken Bi-rich

Table 4 Energies required under tensile test

Alloys	UTS	EL	Energy				Energy index
			Elastic	Plastic		Total	
				Before UTS	After UTS		
Sn	12	62	Negligible	360.15	196	556.15	744
Sn-17Bi	77	39.6	93.49	364.3	729.7	1187.49	3049.2
Sn-50Bi	70	25	69.1	251.3	256.4	576.8	1750
Sn-58Bi	58	19.6	65.53	175.54	262.93	504.13	1136.8

phase occurs on the sample surface as shown in Fig. 12c. The fracture surface of the tensile test sample displays a brittle mode with broken Bi-rich phase seen (Fig. 12e).

Figure 12 d shows the force-displacement curve of tensile test. It shows that the most of the plastic deformation of Sn-58Bi alloy could be ascribed to the deformation after necking. That is, the Bi-rich phase who blocks the Sn-rich phase deformation contributes a lot to the plastic property of Sn-58Bi alloy. And the total energy required for breaking the tensile sample is about 504.13 N·mm.

In the process of tensile test, the energy required to overcome the deformation can be obtained by integrating the force on the whole displacement, as the shadow area in gray color shown in Figs. 9 and 10 in the corresponding displacement-force curves. And the total energy needs during tensile test are listed in Table 3. According to the deformation forms of materials: elastic deformation, even plastic deformation, and non-even deformation after necking, the energy required in the tensile process can be divided into elastic property, even plastic deformation energy and non-even deformation energy after necking. The area under the corresponding displacement-force curve is the energy of the corresponding part, as shown in Table 4. It is found that the homogeneous deformation ability of Sn-Bi alloy becomes worse, and the inhomogeneous transformation takes up the main part of the deformation, compared with the pure tin alloy. And Sn-17Bi is the alloy with the largest energy requirement among all alloys. Its strength and plasticity are excellent.

We may as well multiply UTS and elongation to get a comprehensive index of strength and plasticity, energy index. This index may be more proper to value the comprehensive behavior for engineering mechanical behavior of alloys.

4 Conclusions

Based on the experimental results and discussion above, the following conclusions can be drawn.

1. The microstructure of Sn- x ($x = 10, 17$) Bi alloy is constituted by Bi particle and beta-Sn phase under water cooled condition. The microstructure of Sn-20Bi and Sn-40Bi alloy consists of both eutectic and primary

phases. Sn-50Bi solder contains Sn-Bi eutectic base decorated by beta tin with Bi particles. The thermal DSC curves explain the microstructure formation clearly. The shape of precipitated Bi particle is related to the cooling rate, sphere under water cooled and short rod-like under air-cooled condition.

2. Sn-17 Bi alloy displays the highest strength, better elongation, and needs the most energy in the tensile process of all the Sn- x Bi alloys. Bi particles and a small part of Sn-Bi eutectic being the strengthening particles to intensify beta tin base for Sn-17Bi solder. The beta tin base deformation based on the grain boundary diffusion similar to pure beta tin deformation under the same condition.
3. For Sn-58Bi alloy, the deformation mainly resulted by the grain boundary sliding during even deformation stage and the phase sliding between Bi-rich and Sn-rich phase boundary after necking. And the latter accounts for the majority. Sn-50Bi alloy, in contrast, contains tin phase with dispersion distributed Bi particles. These tin-rich phases work as floating grains, do not participate in the deformation, but provide sliding interfaces with the eutectic part, which promotes the continuous plastic deformation.

Funding This study was funded by Yunnan Science and Technology Major Project (grant number 2019ZE001) and the Research and Development Funding of Yunnan Tin Group (Holding) Co, Ltd.

Data availability The data used to support the findings of this study are available from the corresponding author upon request.

Declarations

Conflict of interest The authors declare that they have no conflict of interest.

References

1. Cheng S, Huang C, Pecht M (2017) A review of lead-free solders for electronics applications. *Microelectron Reliab* 75:77–95
2. Gao N et al (2017) The effect of the material and size of the flip-chip plastic package on warping, in 18th International Conference on Electronic Packaging Technology (ICEPT) p. 352–356

3. Hu M, Kresge L, Lee N (2013) Low-cost high-reliability assembly of thermally warped PoP with novel epoxy flux on solder paste, in 14th International Conference on Electronic Packaging Technology (ICEPT). p. 173–181
4. Powers TA, Singler TJ, Clum JA (1994) Role of tin content in the wetting of Cu and Au by tin-bismuth solders. *J Electron Mater* 23:773–778
5. Morgana Ribas, Anil Kumar, Divya Kosuri, Raghu R. Rangaraju, Pritha Choudhury, Suresh Telu, Siuli Sarkar (2017) Low temperature soldering using Sn-Bi alloys, in Proceedings of SMTA International. Rosemont, IL, USA
6. Morgana Ribas, Tom Hunsinger, Traian Cucu, Ramakrishna H V, Garian Lim, Mike Murphy (2018) (The printed circuit assembler's guide to...™ -) Low-temperature soldering, BR Publishing, Inc. eBook ISBN:978-0-9998648-4-5
7. Hu FQ et al (2018) Influences of Ag addition to Sn-58Bi solder on SnBi/Cu interfacial reaction. *Mater Lett* 214:142–145
8. Li Y et al (2016) Improving the mechanical performance of Sn57.6Bi0.4Ag solder joints on Au/Ni/Cu pads during aging and electromigration through the addition of tungsten (W) nanoparticle reinforcement. *Mater Sci Eng: A* 669:291–303
9. Wu X et al (2017) Microstructure and mechanical behavior of Sn-40Bi-xCu alloy. *J Mater Sci: Mater Electron* 28(20):15708–15717
10. Zhang H, Sun F, Liu Y (2019) Thermal and mechanical properties of micro Cu doped Sn58Bi solder paste for attaching LED lamps. *J Mater Sci: Mater Electron* 30(1):340–347
11. Kanlayasiri K, Kongchayasukawat RH (2018) Property alterations of Sn-0.6Cu-0.05Ni-Ge lead-free solder by Ag, Bi, In and Sb addition. *Trans Nonferrous Met Soc China* 28(6):1166–1175
12. Zhu W et al (2019) Improved microstructure and mechanical properties for SnBi solder alloy by addition of Cr powders. *J Alloy Compd* 789:805–813
13. Nan C et al (2017) Measurement and modeling of phase equilibria for Sb-Sn and Bi-Sb-Sn alloys in vacuum distillation. *Fluid Phase Equilib* 442:62–67
14. Zhang C et al (2014) Effect of Sb content on properties of Sn-Bi solders. *Trans Nonferrous Met Soc China* 24(1):184–191
15. Ma D, Wu P (2016) Improved microstructure and mechanical properties for Sn58Bi0.7Zn solder joint by addition of graphene nanosheets. *J Alloys Compd* 671:127–136
16. Zhu QS et al (2009) Effect of Zn addition on microstructure of Sn-Bi joint, in 2009 International Conference on Electronic Packaging Technology & High Density Packaging (ICEPT). Beijing, China, p. 1043–1046
17. Wang XJ et al (2014) Effect of doping Al on the liquid oxidation of Sn-Bi-Zn solder. *J Mater Sci: Mater Electron* 24:2297–2304
18. Chen X et al (2015) Effect of In on microstructure, thermodynamic characteristic and mechanical properties of Sn-Bi based lead-free solder. *J Alloy Compd* 633:377–383
19. Kim SH et al (2017) Thermo-mechanical evolution of ternary Bi-Sn-In solder micropowders and nanoparticles reflowed on a flexible PET substrate. *Appl Surf Sci* 415:28–34
20. Li Q et al (2016) Characterization of low-melting-point Sn-Bi-In lead-free solders. *J Electron Mater* 45(11):5800–5810
21. Wu X et al (2020) Effect of In addition on microstructure and mechanical properties of Sn-40Bi alloys. *J Mater Sci* 55(7):3092–3106
22. Zhao J et al (2004) Influence of Bi on microstructures evolution and mechanical properties in Sn-Ag-Cu lead-free solder. *J Alloy Compd* 375(1):196–201
23. Zhang XP et al (2007) Creep and fatigue behaviors of the lead-free Sn-Ag-Cu-Bi and Sn60Pb40 solder interconnections at elevated temperatures. *J Mater Sci: Mater Electron* 18(6):665–670
24. Olofinjana A et al (2019) Studies of the solidification characteristics in Sn-Ag-Cu-Bi solder alloys. *Procedia Manuf* 30:596–603
25. Zhao G, Wen G, Sheng G (2017) Influence of rapid solidification on Sn-8Zn-3Bi alloy characteristics and microstructural evolution of solder/Cu joints during elevated temperature aging. *Trans Nonferrous Met Soc China* 27(1):234–240
26. El-Daly AA, Ibrahiem AA (2018) The role of delayed elasticity and stress relaxation in Sn-Bi-Cu lead-free solders solidified under permanent magnet stirring. *J Alloy Compd* 740:801–809
27. Lai Z, Ye D (2016) Microstructure and properties of Sn-10Bi-xCu solder alloy/joint. *J Electron Mater* 45(7):3702–3711
28. Silva BL, Garcia A, Spinelli JE (2017) Complex eutectic growth and Bi precipitation in ternary Sn-Bi-Cu and Sn-Bi-Ag alloys. *J Alloy Compd* 691:600–605
29. Takao H, Yamada A, Hasegawa H (2004) Mechanical properties and solder joint reliability of low-melting Sn-Bi-Cu lead free solder alloy. *R&D Rev Toyota CRDL* 39(2):41
30. Peng C et al (2011) Influence of minor Ag nano-particles additions on the microstructure of Sn30Bi0.5Cu solder reacted with a Cu substrate. *J Mater Sci: Mater Electron* 22(7):797–806
31. Zhang L, Sun L, Guo Y (2015) Microstructures and properties of Sn58Bi, Sn35Bi0.3Ag, Sn35Bi1.0Ag solder and solder joints. *J Mater Sci: Mater Electron* 26(10):7629–7634
32. Zang L et al (2012) Spreading process and interfacial characteristic of Sn-17Bi-0.5Cu/Ni at temperatures ranging from 523K to 673K. *Colloids Surf A: Physicochem Eng Asp* 414:57–65
33. Zhou H et al (2021) Effect of Laser Power on Microstructure and Micro-Galvanic Corrosion Behavior of a 6061-T6 Aluminum Alloy Welding Joints. *Metals* 11(31)
34. Abd El-Salam F et al (2009) Thermally induced variations in structural and mechanical properties of rapid solidified Tin-based alloys. *Mater Sci Eng, A* 506(1–2):135–140
35. Zhang QK et al (2017) Viscoplastic creep and microstructure evolution of Sn-based lead-free solders at low strain. *Mater Sci Eng, A* 701:187–195
36. Qiao YX, Corrosion YPC (2021) Behavior of a Nickel-free high-nitrogen stainless steel with hydrogen charging. *JOM* <https://doi.org/10.1007/s11837-021-04569-2>
37. Kerr M, Chawla N (2004) Creep deformation behaviour of Sn-3.5Ag solder at small length scales. *JOM* 56(6):50–54
38. Kerr M, Chawla N (2004) Creep deformation behavior of Sn-3.5Ag solder/Cu couple at small length scales. *Acta Mater* 52(15):4527–4535
39. Okkerse B (1954) Self-diffusion in lead. *Acta Metall* 2:551–553
40. Ding Y et al (2006) In situ TEM observation of microcrack nucleation and propagation in pure tin solder. *Mater Sci Eng, B* 127(1):62–69
41. Qiao Y et al (2021) Effect of hydrogen charging on microstructural evolution and corrosion behavior of Ti-4Al-2V-1Mo-1Fe alloy. *J Mater Sci Technol* 60:168–176
42. Han J, Guo F (2019) Double tricrystal nucleation behavior in Pb-free BGA solder joints. *Microelectron Reliab* 98:1–9

Publisher's Note Springer Nature remains neutral with regard to jurisdictional claims in published maps and institutional affiliations.